iScience

CellPress
OPEN ACCESS

Article

In situ health monitoring of multiscale structures and its instantaneous verification using mechanoluminescence and dual machine learning

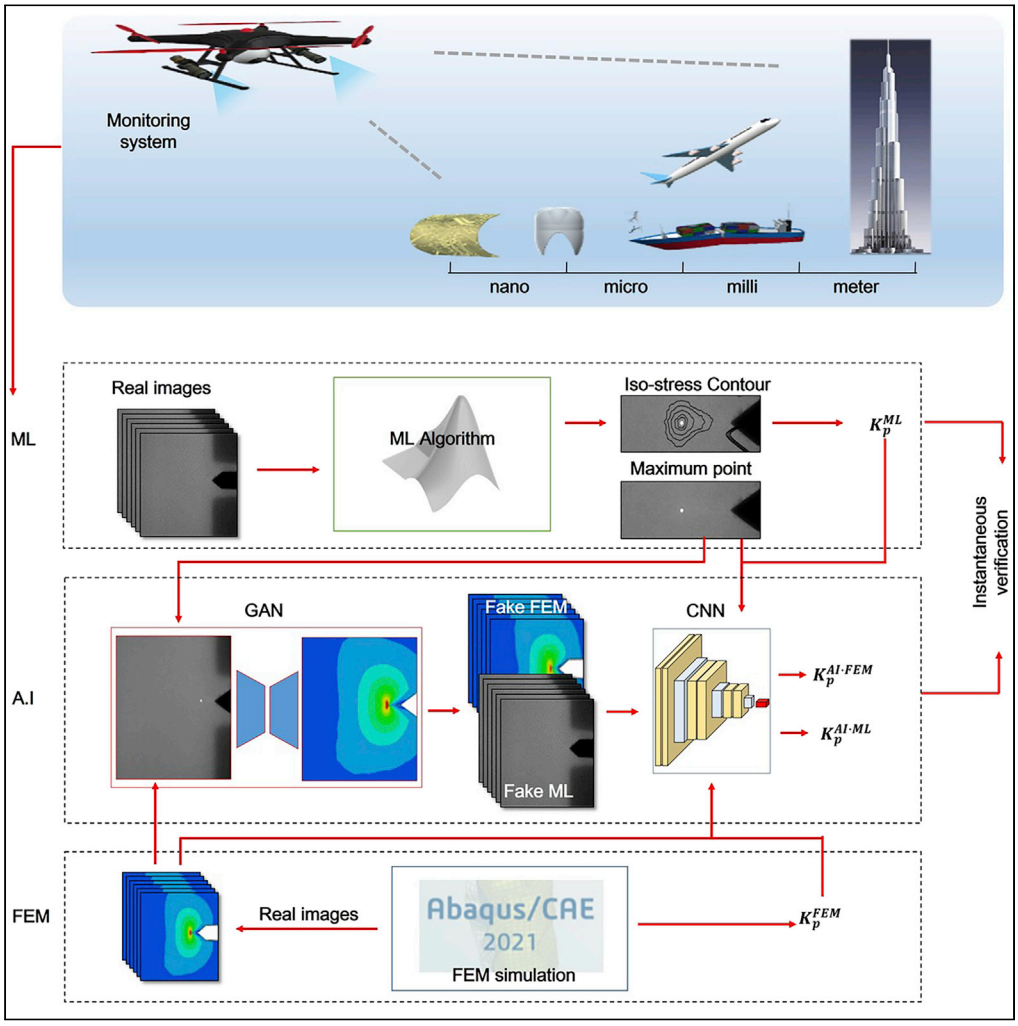

Seong Yeon Ahn, Suman Timilsina, Ho Geun Shin, ..., Yong Nam Kwon, Kwang Ho Lee, Ji Sik Kim

kyn1740@kims.re.kr (Y.N.K.)
khl@knu.ac.kr (K.H.L.)
jisikkim@knu.ac.kr (J.S.K.)

Highlights

Evaluated the significance of existing crack using mechanoluminescence in SrAl2O4:Eu,Dy

Trained GAN generated fake finite element method and mechanoluminescence images

CNN postulated precise plastic stress intensity factor from fake images

Demonstrated *in situ* SHM and its instantaneous verification using ML and dual AI

Ahn et al., iScience *26*, 105758
January 20, 2023
https://doi.org/10.1016/j.isci.2022.105758

iScience

CellPress
OPEN ACCESS

Article

In situ health monitoring of multiscale structures and its instantaneous verification using mechanoluminescence and dual machine learning

Seong Yeon Ahn,[1,7] Suman Timilsina,[1,7] Ho Geun Shin,[2] Jeong Heon Lee,[3] Seong-Hoon Kim,[3] Kee-Sun Sohn,[4] Yong Nam Kwon,[5,*] Kwang Ho Lee,[6,*] and Ji Sik Kim[1,8,*]

SUMMARY

Extensive changes in the legal, commercial and technical requirements in engineering fields have necessitated automated real-time structural health monitoring (SHM) and instantaneous verification. An integrated system with mechanoluminescence (ML) and dual artificial intelligence (AI) modules with subsidiary finite element method (FEM) simulation is designed for *in situ* SHM and instantaneous verification. The ML module detects the exact position of a crack tip and evaluates the significance of existing cracks with a plastic stress-intensity factor (PSIF; K_P). ML fields and their corresponding K_P^{ML} values are referenced and verified using the FEM simulation and bidirectional generative adversarial network (GAN). Well-trained forward and backward GANs create fake FEM and ML images that appear authentic to observers; a convolutional neural network is used to postulate precise PSIFs from fake images. Finally, the reliability of the proposed system to satisfy existing commercial requirements is validated in terms of tension, compact tension, AI, and instrumentation.

INTRODUCTION

Since the enforcement of the "Corporate Manslaughter and Corporate Homicide Act 2007" on April 6, 2008 in the UK,[1] many countries such as New Zealand in 2016, India in 2020, and South Korea in 2021 implemented similar but strengthened legislations. According to the monumental law, the chief executive officers (CEOs) and companies and organizations in these countries can be found guilty of corporate manslaughter when serious management failures result in the gross breach of the duty of care.[2]

This significant change in the legal requirements of companies has inevitably created a new commercial demand for structural safety diagnosis in various industrial fields related to materials, mechanical, aerospace, architecture and civil engineering. Although several high cost, cumbersome methodologies such as Moiré patterns, interferometry, holography, and infrared thermography and conventional nondestructive testing methods have been utilized for detecting and evaluating cracks; they are not real time, noncontacting, multiscale, global full-field, or direct measurement for structural maintenance.[3–6] Furthermore, it is true that none of these techniques can be used for *in situ* inspection and verification under the chaotic condition of construction. Therefore, the law further emphasizes the need for *in situ* structural health monitoring (SHM) during construction as well as the maintenance of large buildings and complex structures. For example, the construction license of a major builder, the "Hyundai Development Company (HDC)," was canceled immediately after the enforcement of the law in South Korea, and its CEO had to resign for further legal punishment because of the deadly collapse of buildings under construction in February 2022. Moreover, HDC is expected to refine the construction plan, which costs an additional $150 million, because the company has to rebuild all eight buildings and provide subsidies to the residents for the construction delay; this emphasizes the industrial importance of *in situ* SHM during construction.[7]

Therefore, we suggest automated real-time and full-field SHM and its instantaneous verification based on mechanoluminescence (ML) in $SrAl_2O_4$:Eu,Dy (SAO)[8–18] and dual machine learning combining a generative adversarial network (GAN)[19,20] and convolutional neural network (CNN) to meet the legal, commercial, and technical requirements in engineering fields.[21,22] Algorithmic MATLAB coding on the ML phenomenon, which is proportional light emission from any mechanical stimulus such as tension,[10] shear,[11]

[1]Kyungpook National University, School of Nano & Advanced Materials Engineering, Kyeongbuk 37224, Republic of Korea

[2]Kyungpook National University, Department of Advanced Science and Technology Convergence, Kyeongbuk 37224, Republic of Korea

[3]Kyungpook National University, Department of Software, Kyeongbuk 37224, Republic of Korea

[4]Sejong University, Nanotechnology and Advanced Materials Engineering, 209 Neungdong ro, Gwangjin-gu, Seoul 143-747, Republic of Korea

[5]Korea Institute of Materials Science, Department of Digital Platform, Changwon 51508, Republic of Korea

[6]Kyungpook National University, Department of Automotive Engineering, Kyeongbuk 37224, Republic of Korea

[7]These authors contributed equally

[8]Lead contact

*Correspondence: kyn1740@kims.re.kr (Y.N.K.), khl@knu.ac.kr (K.H.L.), jisikkim@knu.ac.kr (J.S.K.)

https://doi.org/10.1016/j.isci.2022.105758

compression,[12] torque,[13,14] vibration,[15] friction,[16] and fracture,[17,18] was developed for automatically identifying and evaluating *in situ* cracks from the acquired ML images in elastoplastic structures. GAN is a specialized technique for image generation and restoration, followed by CNN, and it was adopted for the immediate verification of mechanoluminescent stress field images at the crack tip and their singularity K_p^{ML} values. The finite element method (FEM) was used to create training and test sets comprising images of the crack-tip stress field for the GAN and reference values of K_p^{FEM} for the CNN.

Despite the ML phenomenon being discovered four centuries ago, the discovery of SAO by Xu and coworkers 20 years ago has ignited the ML research.[12] For the last two decades, several organic and inorganic ML materials have been reported in addition to a solid understanding on the ML mechanism[23–26]; only few are commercially available.[8,9] For example, SAO is easily available in the market and is also inexpensive. Thus, many researchers have considered ML in SAO, and they reported the potential of ML technology in crack-tip position identification, crack-tip stress field and strain field visualization in elastic and plastic regions, crack path prediction based on the crack-tip effective stress field, hidden crack identification in pressurized hydrogen fuel cells, life-time based performance, and so on.[8,9] Moreover, there are important properties such as reproducible ML, bright emission, ML spectra in human vision range (green), multi-mechanosensitivity, and linear response to applied mechanical stimuli that make SAO a potential candidate for strain engineering.[9] Thus, SAO has been selected in this work because of commercial availability, wide application in strain engineering, and optimal mechano-optical properties.

RESULTS

In situ SHM based on ML module

Figure 1A shows the elastoplastic ML response of the SAO-acrylic composite from the tension specimen under the crosshead speed of 0.05 mm/s using an experimental condition of continuous wave ultraviolet (CW-UV) light illumination above the critical ML power density. The inset of the figure indicates sequential real-time ML images of the gauged section in the tension sample recorded by the high-speed camera during loading. The representative image of the compact tension (CT) specimen under the condition of quasi-dynamic fracture under the same loading and UV exposure conditions is shown Figure 1B, where the white dot represents the moving crack-tip position acquired from the coordinates of the maximum intensity pixel. Figure 1C shows the visualization of the crack-tip stress field based on ML mechanics under the condition of quasi-dynamic fracture. Figures 1A–1C shows that the CW-UV light excitation effectively provides the initial condition for ML excitation and allows the acquisition of a set of calibrated ML images under normal tension and CT. As proven for uniaxial cyclic tension within an elastic region,[27] normal tension up to the yield stress shown in Figure 1A, which exhibits a well-defined linear relationship between the applied tensional stress and instantaneous incremental ML intensity. Figures 1B–1C shows that the visualization of the two-dimensional far field in front of the crack tip is almost impossible because the sensitivity corresponding to the slope of the tensional ML graph below the yield point in Figure 1A is relatively poor. An expensive intensified camera system is required to ensure that the elastic field is visible through ML; this can overcome the commercial and empirical challenges in applying the ML technology to the elastic region.

However, the linearity can be extended to a plastic field with dramatically enhanced sensitivity using an appropriate elastoplastic ML paint or skin,[28] as shown in Figure 1A. This improvement in the ML material parameters can help visualize the two-dimensional evolution of a plastic field near a crack tip via the use of a commercial-grade, non-intensified camera, as demonstrated in Figure 1C. Furthermore, Figure 1C shows the two sets of images of CT testing that indicate the typical evolution of the plastic field in front of a crack tip and crack propagation through ML, which implies the uniform distribution of SAO phosphors in the acrylic composite. The high-speed camera is selected not to achieve higher camera sensitivity but to increase the amount of data collected for GAN and CNN. Considering the short exposure time when using high-speed photography, conventional imaging devices can satisfy the technical requirements for ordinary ML visualization. Therefore, an inexpensive drone equipped with a high-definition camera and UV lamp can be deployed for conducting various standard ML inspections. The visualized images in Figures 1D and S1A–S1D are obtained using a commercial smartphone such as the Galaxy S8; this proves that the performance of a conventional camera is sufficient to capture the plastic ML response and analyze the structural integrity under identical measurement conditions because of the enhanced sensitivity of the ML in the plastic deformation region.

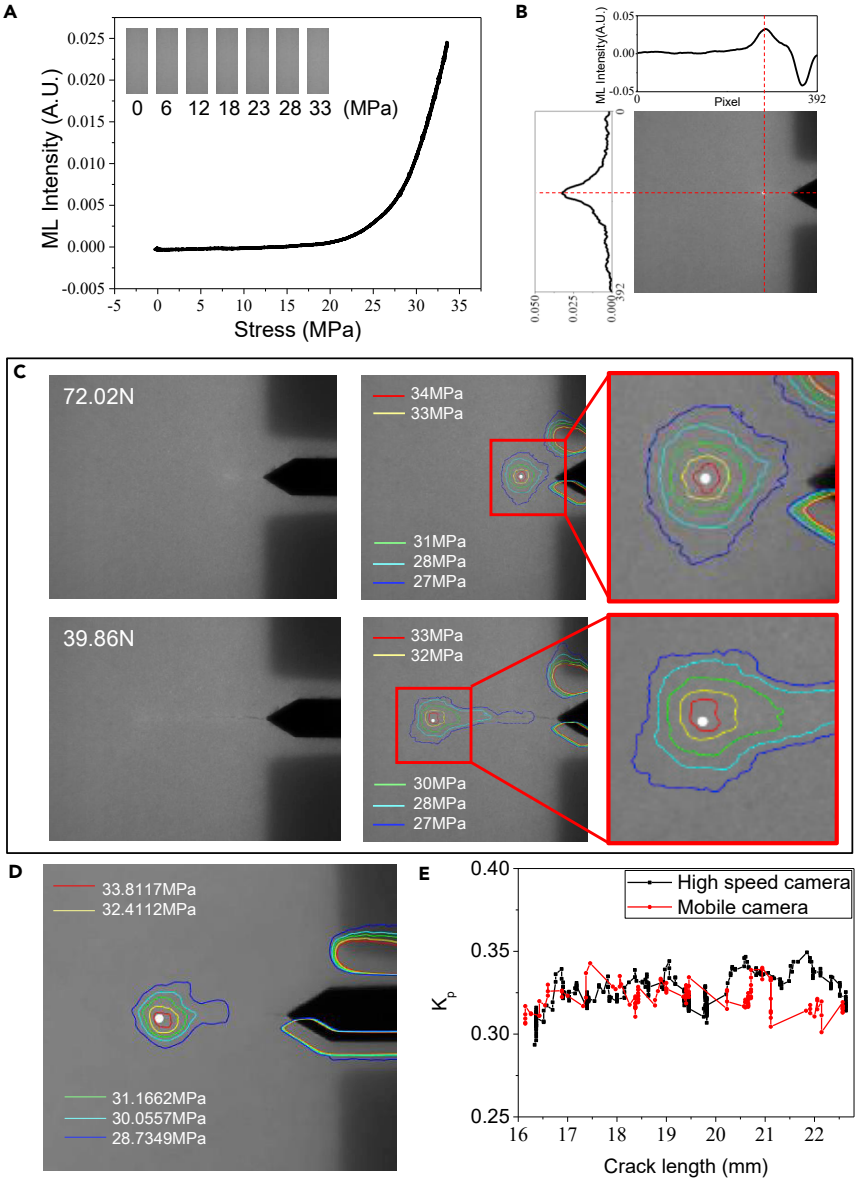

Figure 1. Measurement of plastic stress intensity factors (PSIFs) based on ML mechanics

(A) Calibrated relationship between ML intensity (arbitrary unit) and effective stress (MPa) determined from the uniaxial tension test. The inset of the figure shows the sequential real-time ML images of the gauged section of the tension sample recorded by the high-speed camera while loading.

(B) Crack tip indicated by a white dot; the crack tip is determined by considering that the maximum intensity point coincides with the crack tip attributed to the maximum stress concentration in the region.

(C) Real-time sequential gray ML images of the compact tension (CT) specimen recorded by a high-speed camera; this demonstrates crack propagation while loading (left column), isostress contours in the vicinity of the crack tip (middle column), and their enlarged view in the right column. Isostress contours are obtained from their corresponding isointensity contours with the aid of the calibrated curve shown in (A).

(D) Isostress contours in the vicinity of the crack tip of the CT specimen recorded by a mobile camera.

(E) Comparison of PSIFs obtained from a high-speed camera and a smartphone for different crack lengths. The unit of K_P is $m^{1/5}$.

Thus, ML software based on fracture mechanics for the automated evaluation of ML responses indicates a substantial breakthrough in the field of *in situ* SHM. Figures 1B and 1C show that the new MATLAB software described in Supplementary Code 1 successfully identifies the maximum ML intensity position of a plastic

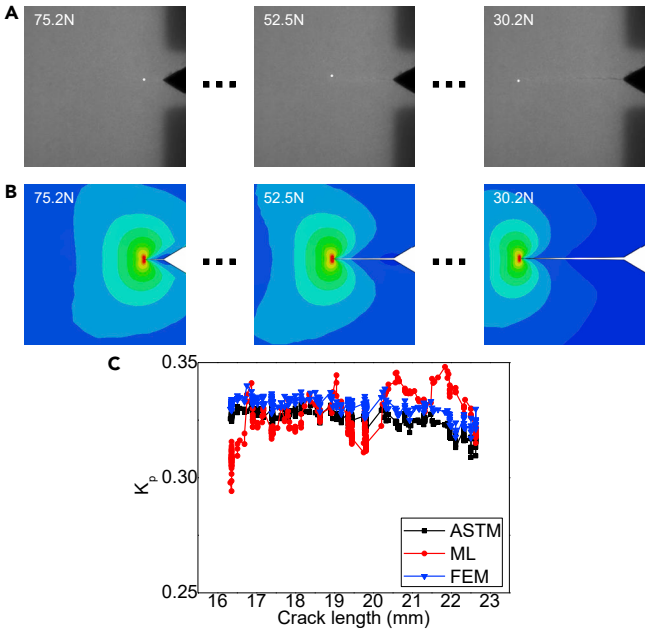

Figure 2. ML images and their corresponding FEM-simulated images

(A) Sequential ML images recorded by high-speed camera while loading, where the white dot represents the crack-tip position on each image.

(B) FEM-simulated images corresponding to each ML image in (A).

(C) Comparison of PSIFs obtained through ML, FEM, and ASTM. The unit of K_P is $m^{1/5}$.

crack tip and its isointensity contour patterns during CT. Then, the standard effective stresses in accordance with the *in situ* isochromatic ML intensities in Figure 1C can be extracted from the results of the uniaxial tension. The plastic SIF (K_p^{ML}) shown in Figure 1E can be conveniently calculated using ML software that generates automatic measurements of the length between the crack tip and the farthest points on a given fringe loop in the instantaneous mechanoluminescent isointensity contours near the crack tip, as well as the corresponding angles of inclination of this line to the crack axis. K_p^{ML} measured from the images acquired using the high-speed camera and mobile camera showed similar results in terms of mean PSIF. Considering the temporal sensitivity of ML technology, the local mismatch of K_p^{ML} between the calculated values from high speed and the mobile phone cameras during crack propagation are very natural. Global accordance between the K_p^{ML} vales of those two supports the reliability of ML technology even when the normal HD camera is used. The magnitude and shape of the stress field of the crack tip predicted by the ML software shown in Figure S2 indicate excellent agreement with the empirical ML isochromatic patterns used to determine K_p^{ML} from the ML intensity. For a more specific understanding of the core logic of numerical calculations obtained using the ML software, the constitutive equation and specific parameters used for the quantification of plastic ML singularity within a near field under the mixed mode are presented in the STAR Methods.

FEM for complementary and reference data

An FEM simulation was conducted for supporting the ML and artificial intelligence (AI) modules to create a set of stress field images at the crack tip and to provide reference values of the plastic stress intensity factor (PSIF; K_p^{FEM}) for training the GAN and CNN. The ML images and their corresponding FEM-simulated images are depicted in Figures 2A and 2B, respectively. The FEM produces a specific visualization of where the structure is distorted, which helps demonstrate the distribution of stresses and strains, regardless of the elastic or plastic deformation. Therefore, the use of this powerful simulation method helps significantly improve the learning quality of the GAN and CNN because of the mutual comparison of the crack-tip stress fields in addition to the plastic SIF values in ML and FEM. Furthermore, the FEM software provides extensive options in the simulations to control the complexity of modeling and analysis. In other words, the desirable level of accuracy in the training dataset, which is associated with the learning cost of GAN or CNN, can be achieved without restriction. The introduction of the FEM software substantially decreases the time

required to obtain the formulaic data from the simulated results for accelerating the training process of AI. These factors imply that the FEM software in conjunction with the ML code shown in Supplementary Code 1 can permit the entire design of the datasets to be constructed, refined, and optimized for training a GAN and CNN even before an object is retrieved or is in use. Thus, the advantages of the complementary FEM include improved insight into the critical parameters of the learning and test data, enhanced learning efficiency, and increased accuracy of the GAN and CNN results.

The evolution of plastic SIF shown in Figure 2C should be discussed based on the comparative consideration between the ML measurement and referenced FEM result for a quasi-dynamic fracture under CT. General trends and mean values of K_p^{ML} and K_p^{FEM}s show acceptable agreement; however, the fluctuation is higher in K_p^{ML} because it is slightly more sensitive to crack propagation than K_p^{FEM}. This phenomenon can reflect the interference exerted by a propagating crack on the stress field in front of the crack tip. The enhanced speed of crack propagation disturbs the crack-tip stress field, and its influence becomes more significant with an increase in crack speed.[29,30] Therefore, time resolution using the ML technology has allowed the quantification of the local fluctuation in a plastic stress field under high-speed imaging conditions. This suggests that the ML technology may be too sensitive to allow the effective monitoring of quasi-dynamic structural health because the temporal resolution obtained by ML is dependent on the trap-releasing process of electrons or holes in the SAO,[8] which is equivalent to at least one microsecond. The perfect match between K_p^{FEM} and K_p^{ASTM}, which was calculated in accordance with an analytical method using ASTM E399 for mode I fracture, also supports the above supposition. Hence, the less sensitive K_p^{FEM} in Figure 2C can be expected to improve the stability of the AI verification module, which is attributed to a more stable and reliable training dataset, faster and less expensive data design, and increased data productivity of the FEM.

Real-time verification using dual AI module

GAN is an unsupervised machine learning algorithm wherein two neural networks compete in a zero-sum game framework, where the generative network creates the candidates and the discriminative network evaluates them (Figure 3A). When a known dataset is applied to the discriminator as the initial training data, the training involves providing it with examples from the selected training dataset until it achieves the desired accuracy. In contrast, the generator is seeded with randomized input from a predefined latent space and trained based on whether it succeeds in fooling the discriminator. Thereafter, candidates created by the generator are evaluated by the discriminator, which involves a deconvolutional and convolutional neural network.[31–33] The bidirectional and interactive structure of a GAN can provide the possibility of simultaneous verification of the FEM simulation and ML measurement, as depicted in Figures 3B and 3C. Two different GAN models are trained to generate fake images, where the GAN generating the fake FEM image (Figure 3B) is referred to as the forward GAN, and that generating the fake ML image (Figure 3C) is referred to as the backward GAN. The specific architectures of the GAN generator and discriminator are presented in Figures S3 and S4, respectively; the code is presented in Supplementary Code 2.

Furthermore, the CNN is a deep learning technique that is mostly utilized for analyzing visual imagery. It is frequently applied for the recognition, classification, and analysis of various images and videos.[34–38] A CNN requires relatively lesser preprocessing than that required by other image processing algorithms; this means that the network deciphers the filters. Thus, performance verified via the analysis of various images and independence from the need for prior knowledge and human effort in feature design are major advantages for automating the proper assessment of PSIF values from fake FEM or fake ML images, as shown in Figure 3D. The specific architecture of the CNN is presented in Figure S5, and the code is presented in Supplementary Code 3. The CNN model trained for real FEM images and K_p^{FEM} is referred to as forward CNN, whereas the CNN model trained for real ML images and K_p^{ML} is referred to as backward CNN.

The evolution of the K_p^{AI} values is shown in Figure 3E. The magnitudes of the K_p^{AI} values predicted by the CNNs agree well with those of the experimental and simulated results. However, the fluctuation is higher in $K_p^{AI.ML}$ (backward) than that in $K_p^{AI.FEM}$ (forward) during cracking, which implies that the quality of the generated fake ML photos is sufficient to resemble the local fluctuation in a real crack tip in an ML field under *in situ* failure. Compared to the local deviation presented in Figures 1E, 2C, and 3E show improved local and global accordance, which indicates the solid performances of the FEM and AI module. Moreover, the variation in $K_p^{AI.FEM}$ almost perfectly matches that in K_p^{FEM} when combined with the fake FEM images generated by the GAN; this helps ensure reliable accuracy and high perception in the evaluation of ML based on

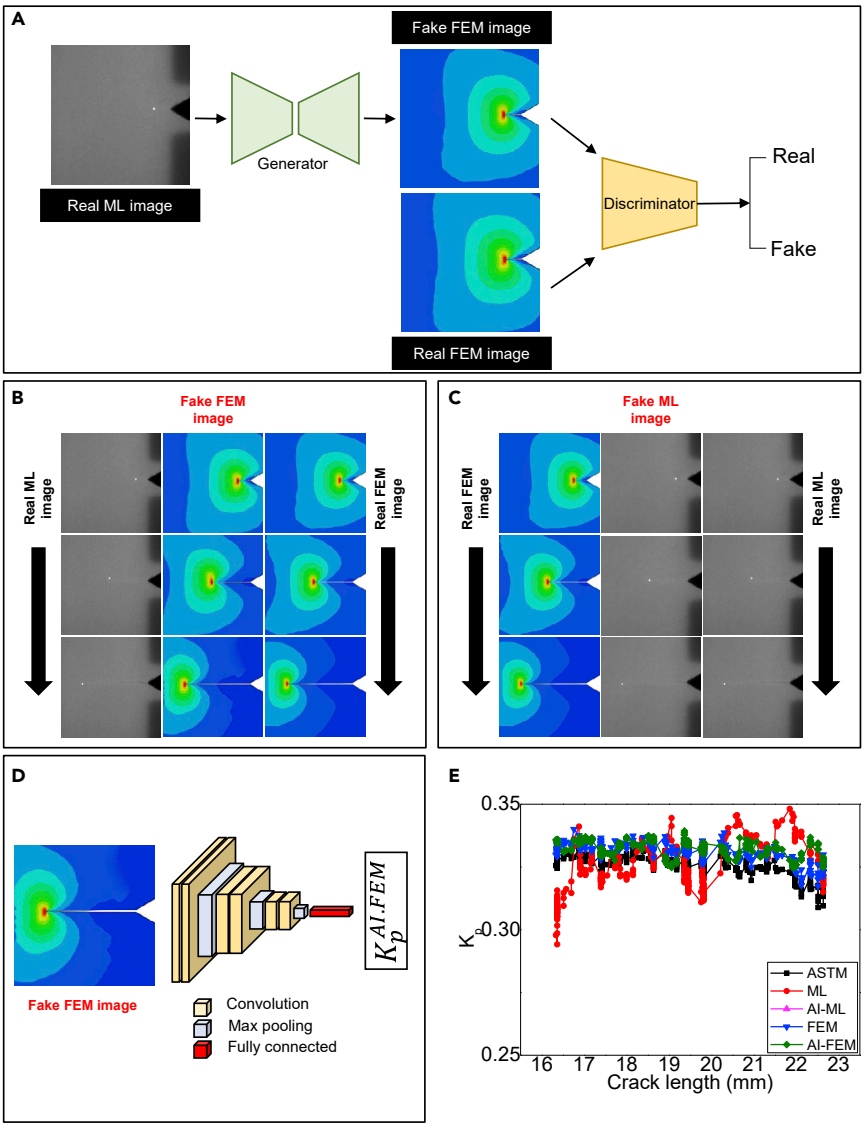

Figure 3. Prediction of PSIF from the dual AI module

(A) GAN network (forward).

(B) Generation of fake FEM images from the trained-forward GAN model.

(C) Generation of fake ML images from the trained-backward GAN model.

(D) CNN network (forward).

(E) Comparison of PSIFs obtained through ML, FEM, ASTM method, forward CNN model (AI.FEM), and backward CNN model (AI.ML). The unit of K_P is $m^{1/5}$.

forward AI routes. Compared with the plastic ML photos shown in Figure 3B, the elastoplastic FEM images provide a greater amount of diverse information that includes far fields in addition to near fields in the vicinity of a crack tip regardless of whether they are simulated using an expensive FEM or created with an inexpensive GAN.

Table 1 summarizes the performance of the proposed system consisting of ML and AI modules for detecting, evaluating, and verifying an artificially introduced mode I crack. Each ML and AI module successfully demonstrates an acceptable performance in terms of detection of cracks, visualization of the crack-tip stress field, and evaluation of the plastic SIF with over 97% accuracy within 2 s; these are key parameters for *in situ* SHM and its instantaneous verification. The ML module makes it possible to visualize only the plastic near-field in front of the crack, whereas the AI module allows the detection of the elastic far-field

Table 1. Performance summary of the detection of crack position, stress resolution in front of the crack tip, accuracy of PSIFs of K_p^{ML}, $K_p^{AI\cdot FEM}$ (forward), and $K_p^{AI\cdot ML}$ (backward), and computational costs of ML and AI modules and reference FEM simulation

Module	Detection of crack tip	Visualization of stress field	Evaluation of K_P (%)	Computational cost (s)
ML	Excellent	Near-field	97	1.6
AI	Excellent	Far- and near-field	98.3 (Backward) 99.2 (Forward)	0.5 (Backward) 0.5 (Forward)
FEM	Excellent	Far- and near-field	Ref.	300

in addition to the plastic near-field. The average deviations of the PSIFs estimated by the forward and backward AI modules from the reference FEM values are slightly reduced when compared with those of ML; this implies that the sophisticated FEM data effectively help the learning processes of the GAN and CNN. Nevertheless, FEM simulation appears to be inappropriate for prompt verification because of the large computation time of over 500 s; this inevitably necessitates the involvement of dual machine learning modules for the immediate verification of the SHM results by ML. In conclusion, the forward AI route appears to satisfactorily meet the commercial requirements for the verification of the ML technology in terms of the stability, accuracy, cost, and perception, as summarized in Table 1.

DISCUSSION

We successfully implemented a novel integrated system involving dual AI composed of a GAN and a CNN in addition to advanced ML mechanics for achieving *in situ* ML measurement and AI verification of structures under construction or operational multiscale structures. However, the reliability of the suggested system must be comprehensively validated in various ways to satisfy the commercial requirements for standard ML hardware and machine learning software. The first method is to ensure plastic ML linearity, irrespective of the loading conditions, in conjunction with the mechanical and microstructural ML constraints. The instantaneous ML intensities with respect to variations in the tensional crosshead speeds are evaluated using mechanical and microstructural approaches. The mechanical analysis in Figure 4A shows that the mechano-optical linearity[39–41] can be reproduced consistently for all loading conditions and extended to a plastic field with a dramatically enhanced level of sensitivity because of the improved ML material, instrumentation, and measurement factors. Furthermore, it is evident in Figure 4A that all plastic stresses follow one master curve regardless of the tensional cross speeds, even if the elastic stresses slightly deviate from the mean value caused by poor sensitivity within the elastic region. Identical results are confirmed by measurements using a photon multiplier tube (PMT), as shown in Figure S6.

Of interest, based on the microstructural analysis of the plastically deformed specimen in Figure 4B, the increased rate of photon emission beyond the yield point is attributed to crazing within the acrylic matrix of the ML paint, which rapidly develops a stress concentration on the SAO particles located near the crazes.[42] A craze that is not detectable on the surface must be discriminated from a crack because it can carry internal or external stresses.[43] Moreover, the evolution of the craze before crack initiation and propagation efficiently absorbs the fracture energy and improves the fracture toughness of the polymer. The initial absorption of energy in the craze region is increased by several hundred times when compared with that of a noncrazed region, which can change the sensitivity of the ML response in an elastoplastic ML composite. Considering that the typical development of crazes near the SAO particles in tension specimens originates from plastic yielding and becomes severe with incremental variations in stress or strain (Figure S7), the hypothesis based on crazing may be the only plausible mechanism for the enhanced sensitivity of an ML composite in a plastic field.

The second method for ensuring reliability is achieving an intrinsic time-resolved resolution of ML and extrinsic concerns about the adequateness of camera sensitivity to capture local fluctuations in photon emissions during CT. Although downgrading the camera sensitivity ensures excellent time resolution of the ML technology in facilitating the measurement of local stress fluctuations at the front of a crack tip, extracted K_p^{ML} values that require evaluation of the crack-tip stress fields can be better analyzed in terms of the maximum intensity based on the variation in the crack length during crack propagation, as indicated in Figure 4C. The variations in K_p^{ML} and the corresponding maximum ML intensity at the crack tip show perfect agreement during crack propagation regardless of the imaging system; e.g., a high-speed camera

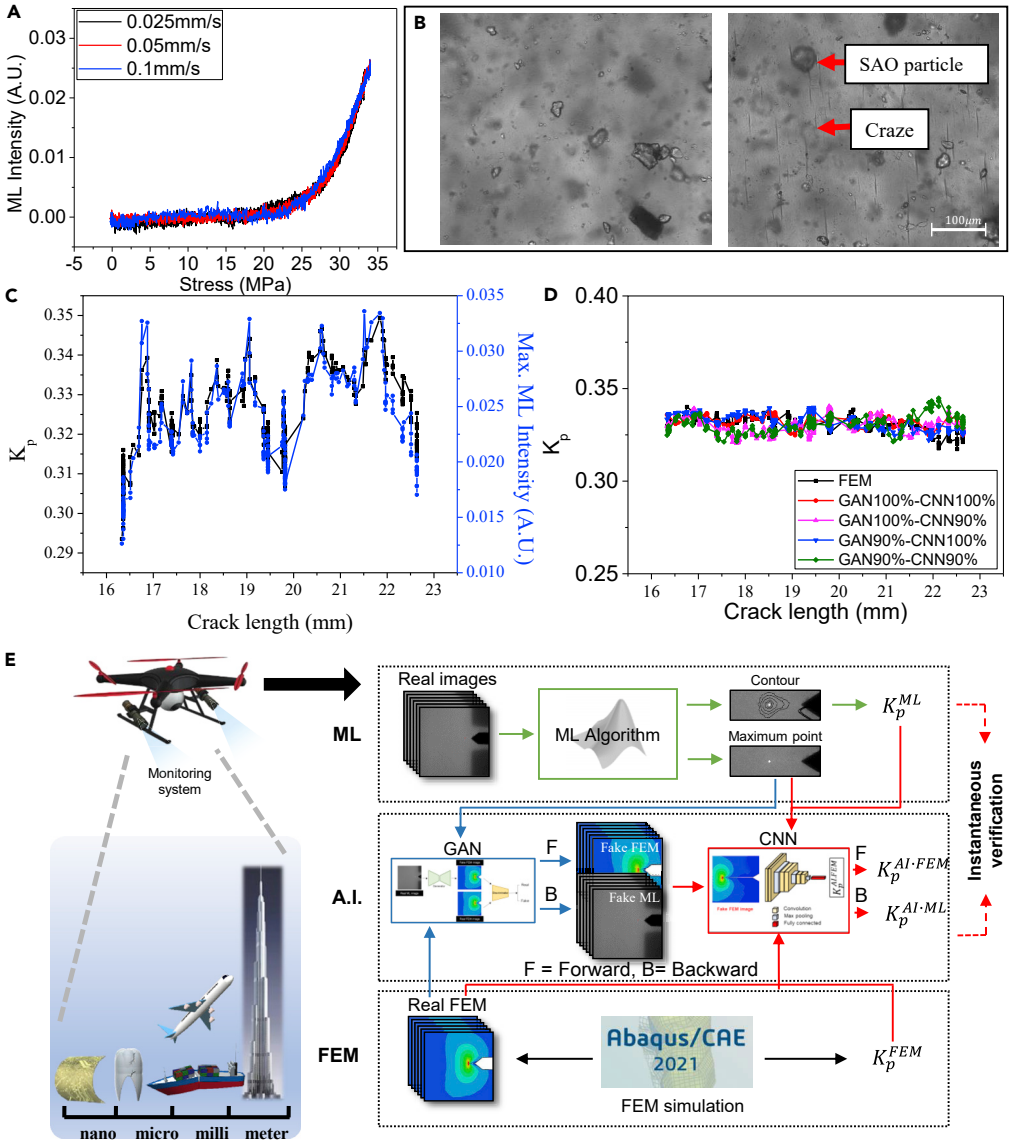

Figure 4. Reliability validation of the suggested system

(A) Identical ML responses despite different loading rates.

(B) Micrographs of the tension sample showing SAO particles and crazes before load application (left) and under stress of 32 MPa (right). The scale bar size is 100 μm.

(C) Variation patterns of K_P and crack tip intensity depicting resemblances.

(D) Comparison of K_p^{FEM}value obtained from FEM with $K_p^{AI\cdot FEM}$ values obtained from four different cases of machine learning. The unit of K_P is $m^{1/5}$.

(E) Schematic of three different methods—AI consisting of GAN and CNN, conventional ML, and FEM—to determine fracture parameters such as PSIF for multiscale structures.

(Figure 4C) or a conventional camera such as a smartphone (Figure S8), which proves the excellent time resolution of the ML evaluation in addition to ML measurement for fracture mechanics.

We also confirmed the performance of dual AI by processing values under various conditions of partial restriction of the training dataset. Four different cases of machine learning either alternatively or simultaneously confine the training of a GAN and a CNN to the forepart in 90% of the training datasets (Figure 4D); these have been analyzed to compare them with the real FEM values. All $K_p^{AI.FEM}$ values predicted by the dual AI agreed with one another and showed acceptable agreement with the FEM results, even in the

tail region of the plastic SIF values where data were excluded; this suggests that an evaluation using dual AI may guarantee reliable accuracy even if the measured ML response is not exactly well-trained. The performances of GAN and CNN can be validated by considering that the accuracy of dual AI can be continuously improved because of the inherent recursive and recurrent characteristics of GAN and CNN given that the accumulation and training of data proceeds while the unified standard ML system is working.

Sequential ML photographs recorded while crack is moving in response to externally applied load can only display the plastic field at the crack tip vicinity under continuous UV irradiation. The plastic field is a valuable asset that can evaluate the significance of existing crack in terms of the plastic stress intensity factor (PSIF); however, the elastic field distributed in a considerably larger area compared to the plastic field is missing because of the poor ML emission in the elastic deformation. The elastic field is an important trait in SHM because it allows the qualitative analysis of full-field stress distribution in the given structure. Thus, GAN plays a crucial role in translating a visually less-informative ML image into visually high-informative fake FEM image. In addition to achieving high-informative fake FEM image from a less-informative ML image, it is important for quantifying the crack-tip stress field in terms of a single fracture parameter such as PSIF. Although PSIF can be determined from the plastic crack-tip field solution, it is computationally expensive, and therefore, it would not favor the *in situ* SHM. Thus, the introduction of CNN is necessary to predict the PSIF for the given ML image to ensure *in situ* SHM.

There is a possibility of extending the present work by considering ML materials other than SAO that show emission under elastic deformation. Both organic and inorganic ML materials with elastico-mechanoluminescence can be used to obtain the ML images containing the information of crack-tip stress field distribution and follow the present framework to train GAN and CNN models. The models trained on one ML material may not work on other ML material because the linearity, strain sensitivity, loading rate effect, ML threshold emission, etc., could vary depending on the material. Thus, GAN and CNN models trained on one ML material may not work on other ML materials.

In conclusion, the novel integrated system shown in Figure 4E satisfies the commercial requirements of reliability and reproducibility for machine learning, as well as that for ML technology; this was validated successfully and comprehensively in terms of tension, CT, AI, and instrumentation. The upper ML module simultaneously detects the exact crack-tip position and crack-tip stress field when a crack exists; further, this module evaluates the significance of the existing crack in terms of the PSIF by using ML images scanned from the target structure. The FEM simulation offers reference results for comparison with a visualized ML crack-tip stress field and the singularity of K_p^{ML} under an identical situation during *in situ* crack propagation. The middle AI module for the verification of the ML data compares the observed ML or simulated FEM images to generate the translated FEM (forward) or ML (backward) images based on well-trained GANs. Furthermore, it estimates the values of $K_p^{AI.FEM}$ (forward) or $K_p^{AI.ML}$ (backward) for the virtual images using additional CNNs.

Limitations of the study

This study is limited to uniaxial loading condition although the mix-mode loading condition is involved in crack initiation and propagation in the real world. A uniaxial loading was opted to make the crack-tip field and crack profile simple because the current study demonstrates the possibility of the novel integrated system for SHM; this allowed GAN and CNN to learn the problem with a small number of images.

In future work, a significantly more complex crack system such as one with a mix-mode loading condition at various degree of loading will be considered, which can allow us to generate a large number of training images for generalizing the complex problem.

STAR★METHODS

Detailed methods are provided in the online version of this paper and include the following:

- KEY RESOURCES TABLE
- RESOURCE AVAILABILITY
  - Lead contact
  - Materials availability
  - Data and code availability

- EXPERIMENTAL MODEL AND SUBJECT DETAILS
- METHODS
  - Sample preparation and experimental setup
  - Evaluation of ML using the MATLAB code
  - FEM simulation
  - Learning for dual AI
  - Solution to determine PSIF from ML isointensity contours

SUPPLEMENTAL INFORMATION

Supplemental information can be found online at https://doi.org/10.1016/j.isci.2022.105758.

ACKNOWLEDGMENTS

This work was supported by a National Research Foundation of Korea (grant funded by the Korean government [grant numbers 2017R1A2B4001877, 2021R1A2C1005732, and 2022R1I1A3052916] and Internal project of Korea Institute of Materials Science supported by NST, project number POC3330.

AUTHOR CONTRIBUTIONS

S.Y.A: Data curation, Formal analysis, Investigation, Methodology, Visualization. S.T.: Data curation, Formal analysis, Investigation, Methodology, Visualization, Writing – Review and Editing. H.G.S.: Data curation, Visualization, Software. J.H.L.: Data curation, Investigation, Software, Visualization. S-H.K.: Investigation, Visualization, Software, Supervision. K-S. S.: Formal analysis, Supervision. Y.N.K.: Resources, Supervision, Writing – Review and Editing. K.H. L.: Resources, Supervision, Writing – Review and editing. J.S.K.: Conceptualization, Formal analysis, Resources, Supervision, Writing – Original draft, Writing – Review and Editing.

DECLARATION OF INTERESTS

The Korean patent number related to this work is 10–2377367 and the authors declare no competing interests.

Received: September 12, 2022
Revised: October 25, 2022
Accepted: December 6, 2022
Published: January 20, 2023

REFERENCES

1. UK Public General Acts. Corporate Manslaughter and Corporate Homicide Act 2007. https://www.legislation.gov.uk/ukpga/2007/19/contents/.

2. Health and S. Executive. About Corporate Manslaughter. https://www.hse.gov.uk/corpmanslaughter/about.htm.

3. Mohan, A., and Poobal, S. (2018). Crack detection using image processing: a critical review and analysis. Alex. Eng. J. *57*, 787–798. https://doi.org/10.1016/j.aej.2017.01.020.

4. Dwivedi, S.K., Vishwakarma, M., and Soni, P. (2018). Advances and researches on non destructive testing: a review. Mater. Today Proc. *5*, 3690–3698. https://doi.org/10.1016/j.matpr.2017.11.620.

5. Liu, H., Zhang, H., Han, W., Lin, H., Li, R., Zhu, J., and Huang, W. (2021). 3D printed flexible strain sensors: from printing to devices and signals. Adv. Mater. *33*, 2004782. https://doi.org/10.1002/adma.202004782.

6. Meneghetti, G., Ricotta, M., and Pitarresi, G. (2019). Infrared thermography-based evaluation of the elastic-plastic J-integral to correlate fatigue crack growth data of a stainless steel. Int. J. Fatigue *125*, 149–160. https://doi.org/10.1016/j.ijfatigue.2019.03.034.

7. The Korea Herald. HDC to Rebuild Collapsed Gwangju Apartment to Restore Public Trust. https://www.koreaherald.com/view.php?ud=20220504000662.

8. Zhang, J.-C., Wang, X., Marriott, G., and Xu, C.-N. (2019). Trap-controlled mechanoluminescent materials. Prog. Mater. Sci. *103*, 678–742. https://doi.org/10.1016/j.pmatsci.2019.02.001.

9. Feng, A., and Smet, A.P.F. (2018). A review of mechanoluminescence in inorganic solids: compounds, mechanisms, models and applications. Materials *11*, 484. https://doi.org/10.3390/ma11040484.

10. Rahimi, M.R., Yun, G.J., and Choi, J.-S. (2014). A predictive mechanoluminescence transduction model for thin-film $SrAl_2O_4$: Eu^{2+}, Dy^{3+} (SAOED) stress sensor. Acta Mater. *77*, 200–211. https://doi.org/10.1016/j.actamat.2014.06.002.

11. Basnet, R., Timilsina, S., Lee, K.H., and Kim, J.S. (2018). Evaluation of the elasto-plastic crack tip singularities via mechano-luminescent effects. Int. J. Eng. Sci. *123*, 127–142. https://doi.org/10.1016/j.ijengsci.2017.11.018.

12. Xu, C.-N., Watanabe, T., Akiyama, M., and Zheng, X.-G. (1999). Direct view of stress distribution in solid by mechanoluminescence. Appl. Phys. Lett. *74*, 2414–2416. https://doi.org/10.1063/1.123865.

13. Kim, G.-W., and Kim, J.-S. (2013). Dynamic torsional response analysis of mechanoluminescent paint and its application to non-contacting automotive torque transducers. Meas. Sci. Technol. *25*, 015009. https://doi.org/10.1088/0957-0233/25/1/015009.

14. Kim, J.S., and Kim, G.W. (2014). New non-contacting torque sensor based on the mechanoluminescence of ZnS: Cu microparticles. Sensor Actuator Phys. *218*, 125–131. https://doi.org/10.1016/j.sna.2014.07.023.

15. Zhan, T., Xu, C.N., Fukuda, O., Yamada, H., and Li, C. (2011). Direct visualization of ultrasonic power distribution using mechanoluminescent film. Ultrason. Sonochem. *18*, 436–439. https://doi.org/10.1016/j.ultsonch.2010.07.017.

16. Matsui, H., Xu, C.N., Liu, Y., and Tateyama, H. (2004). Origin of mechanoluminescence from Mn-activated ZnAl 2 O 4: triboelectricity-induced electroluminescence. Phys. Rev. B *69*, 235109. https://doi.org/10.1103/PhysRevB.69.235109.

17. Li, C., Xu, C.N., Imai, Y., and Bu, N. (2011). Real-time visualisation of the Portevin–Le Chatelier effect with mechanoluminescent-sensing film. Strain *47*, 483–488. https://doi.org/10.1111/j.1475-1305.2009.00713.x.

18. Chandra, B.P., Chandra, V.K., Jha, P., Patel, R., Shende, S.K., Thaker, S., and Baghel, R.N. (2012). Fracto-mechanoluminescence and mechanics of fracture of solids. J. Lumin. *132*, 2012–2022. https://doi.org/10.1016/j.jlumin.2012.03.001.

19. Goodfellow, I., Pouget-Abadie, J., Mirza, M., Xu, B., Warde-Farley, D., Ozair, S., Courville, A., and Bengio, Y. (2020). Generative adversarial networks. Commun. ACM *63*, 139–144. https://doi.org/10.1145/3422622.

20. Isola, P., Zhu, J.Y., Zhou, T., and Efros, A.A. (2017). Image-to-image translation with conditional adversarial networks. Proc. IEEE Conf. Comput. Vis. Pattern Recognit. 1125–1134. https://doi.org/10.1109/CVPR.2017.632.

21. Krizhevsky, A., Sutskever, I., and Hinton, G.E. (2017). Imagenet classification with deep convolutional neural networks. Commun. ACM *60*, 84–90. https://doi.org/10.1145/3065386.

22. Lawrence, S., Giles, C.L., Tsoi, A.C., and Back, A.D. (1997). Face recognition: a convolutional neural-network approach. IEEE Trans. Neural Netw. *8*, 98–113. https://doi.org/10.1109/72.554195.

23. Lu, L., Sun, M., Wu, T., Lu, Q., and Huang, B. (2021). Native point defect modulated Cr 3+–LaAlO 3 as an in vitro excited contrast medium for in vivo near-infrared persistent deep-tissue bio-imaging. Chem. Commun. *57*, 9366–9369. https://doi.org/10.1039/d1cc04064b.

24. Huang, B. (2017). Doping of RE ions in the 2D ZnO layered system to achieve low-dimensional upconverted persistent luminescence based on asymmetric doping in ZnO systems. Phys. Chem. Chem. Phys. *19*, 12683–12711. https://doi.org/10.1039/c7cp01623a.

25. Huang, B., Peng, D., and Pan, C. (2017). Energy Relay Center" for doped mechanoluminescence materials: a case study on Cu-doped and Mn-doped CaZnOS. Phys. Chem. Chem. Phys. *19*, 1190–1208. https://doi.org/10.1039/c6cp07472c.

26. Huang, B. (2016). Energy harvesting and conversion mechanisms for intrinsic upconverted mechano-persistent luminescence in CaZnOS. Phys. Chem. Chem. Phys. *18*, 25946–25974. https://doi.org/10.1039/c6cp04706h.

27. Sohn, K.S., Cho, M.Y., Kim, M., and Kim, J.S. (2015). A smart load-sensing system using standardized mechano-luminescence measurement. Opt Express *23* (5), 6073–6082. https://doi.org/10.1364/OE.23.006073.

28. Shin, H.G., Timilsina, S., Sohn, K.S., and Kim, J.S. (2022). Digital image correlation compatible mechanoluminescent skin for structural health monitoring. Adv. Sci. *9*, 2105889. https://doi.org/10.1002/advs.202105889.

29. Ju, Y., Xie, H., Zhao, X., Mao, L., Ren, Z., Zheng, J., Chiang, F.P., Wang, Y., and Gao, F. (2018). Visualization method for stress-field evolution during rapid crack propagation using 3D printing and photoelastic testing techniques. Sci. Rep. *8*, 4353–4410. https://doi.org/10.1038/s41598-018-22773-0.

30. Arakawa, K., Nagoh, D., and Takahashi, K. (1997). Crack velocity and acceleration effects on dynamic stress intensity factor in polymers. Int. J. Fract. *83*, 305–313. https://doi.org/10.1023/A:1007387417517.

31. Chen, Y., Yang, X.H., Wei, Z., Heidari, A.A., Zheng, N., Li, Z., Chen, H., Hu, H., Zhou, Q., and Guan, Q. (2022). Generative adversarial networks in medical image augmentation: a review. Comput. Biol. Med. *144*, 105382. https://doi.org/10.1016/j.compbiomed.2022.105382.

32. Li, J., Chen, Z., Cheng, L., and Liu, X. (2022). Energy data generation with Wasserstein deep convolutional generative adversarial networks. Energy *257*, 124694. https://doi.org/10.1016/j.energy.2022.124694.

33. Liu, S., Jiang, H., Wu, Z., and Li, X. (2022). Data synthesis using deep feature enhanced generative adversarial networks for rolling bearing imbalanced fault diagnosis. Mech. Syst. Signal Process. *163*, 108139. https://doi.org/10.1016/j.ymssp.2021.108139.

34. Spencer, M., Eickholt, J., and Cheng, J. (2015). A deep learning network approach to ab initio protein secondary structure prediction. IEEE/ACM Trans. Comput. Biol. Bioinform. *12*, 103–112. https://doi.org/10.1109/TCBB.2014.2343960.

35. Mamoshina, P., Vieira, A., Putin, E., and Zhavoronkov, A. (2016). Applications of deep learning in biomedicine. Mol. Pharm. *13*, 1445–1454. https://doi.org/10.1021/acs.molpharmaceut.5b00982.

36. Silver, D., Huang, A., Maddison, C.J., Guez, A., Sifre, L., Van Den Driessche, G., Schrittwieser, J., Antonoglou, I., Panneershelvam, V., Lanctot, M., et al. (2016). Mastering the game of Go with deep neural networks and tree search. Nature *529*, 484–489. https://doi.org/10.1038/nature16961.

37. Schütt, K.T., Arbabzadah, F., Chmiela, S., Müller, K.R., and Tkatchenko, A. (2017). Quantum-chemical insights from deep tensor neural networks. Nat. Commun. *8*, 13890–13898. https://doi.org/10.1038/ncomms13890.

38. Wang, C., Xiong, R., Tian, J., Lu, J., and Zhang, C. (2022). Rapid ultracapacitor life prediction with a convolutional neural network. Appl. Energy *305*, 117819. https://doi.org/10.1016/j.apenergy.2021.117819.

39. Song, H., Timilsina, S., Jung, J., Kim, T.S., and Ryu, S. (2022). Improving the sensitivity of the mechanoluminescence composite through functionalization for structural health monitoring. ACS Appl. Mater. Interfaces *14*, 30205–30215. https://doi.org/10.1021/acsami.2c07286.

40. Kim, J.S., Kibble, K., Kwon, Y.N., and Sohn, K.S. (2009). Rate-equation model for the loading-rate-dependent mechanoluminescence of SrAl 2 O 4: Eu 2+, Dy 3+. Opt. Lett. *34*, 1915–1917. https://doi.org/10.1364/OL.34.001915.

41. Sohn, K.S., Park, W.B., Timilsina, S., and Kim, J.S. (2014). Mechanoluminescence of SrAl 2 O 4: Eu 2+, Dy 3+ under cyclic loading. Opt. Lett. *39*, 1410–1413. https://doi.org/10.1364/OL.39.001410.

42. Williams, M.L. (1952). Stress singularities resulting from various boundary conditions in angular corners of plates in extension. J. Appl. Mech. *19*, 526–528. https://doi.org/10.1115/1.4010553.

43. Arzhakova, O.V., Dolgova, A.A., Yarysheva, L.M., Volynskii, A.L., and Bakeev, N.F. (2015). Specific features of the environmental crazing of poly (ethylene terephthalate) fibers. Polymer *56*, 256–262. https://doi.org/10.1016/j.polymer.2014.11.044.

44. Hutchinson, J. (1968). Singular behaviour at the end of a tensile crack in a hardening material. J. Mech. Phys. Solids *16*, 13–31. https://doi.org/10.1016/0022-5096(68)90014-8.

45. Shih, C.F. (1973). Elastic-Plastic Analysis of Combined Mode Crack Problems (Harvard University).

46. Stepanova, L. (2018). Asymptotic methods and their applications in nonlinear fracture mechanics: a review. J. Phys, Conf. Ser. *1096*, 012058. https://doi.org/10.1088/1742-6596/1096/1/012058.

47. McClintock, F.A. (1971). Plasticity aspects of fracture. In Engineering Fundamentals and Environmental Effects (Elsevier), pp. 47–225.

STAR★METHODS

KEY RESOURCES TABLE

REAGENT or RESOURCE	SOURCE	IDENTIFIER
Chemicals, peptides, and recombinant proteins		
$SrAl_2O_4$:Eu,Dy (SAO)	Nemoto & Co.,Japan	
Acrylic resin powder	Struers ApS (Denmark)	
Deposited data		
Codes	This paper	https://github.com/MechanoluminescenceAI/SHM
Software and algorithms		
Python	python.org	Version 3.6.6
Keras	keras.io	Version 2.2.2
Pandas	pandas.pydata.org	Version 0.23.4
Numpy	numpy.org	Version 1.14.5
Abaqus	simuleon.com	2021
Matlab	mathworks.com	R2016b

RESOURCE AVAILABILITY

Lead contact

Further information and requests for resources and reagents should be directed to the lead contact, Ji Sik Kim (jisikkim@knu.ac.kr).

Materials availability

This study did not generate new unique reagents.

Data and code availability

- All data reported in this paper will be shared by the lead contact on request.
- Supplementary code 1, Supplementary code 2, and Supplementary code 3 used in this work have been deposited at GitHub (https://github.com/MechanoluminescenceAI/SHM) and are publicly available as of the date of publication.
- Any additional information required to reanalyze the data reported in this paper is available from the lead contact upon request.

EXPERIMENTAL MODEL AND SUBJECT DETAILS

Our study does not use experimental models typical in the life sciences.

METHODS

Sample preparation and experimental setup

Green photon-emitting mechanoluminescent $SrAl_2O_4$:Eu,Dy (SAO) with excitation and emission peaks at 360 nm and 530 nm, respectively, were purchased from Nemoto & Co., Japan. Acrylic resin powder, which is optically transparent after hot pressing, was purchased from Struers ApS (Denmark). A mixture of acrylic resin and SAO powder in the ratio of 7:3 by weight percent was homogenously mixed using a milling machine (WiseMix ball mill, DAIHAN, Republic of Korea) to facilitate homogeneous distribution. ZrO_2 balls with diameters of 2–10 mm were used. The homogenous mixture was then hot pressed at 180 °C under 20 MPa using a hot press machine (QM900M, QMESYS, Republic of Korea); this resulted in a rectangular bar with dimensions 45 × 45 × 3 mm (length × breadth × thickness). Finally, a CT specimen was cut from the plate into a defined shape and size based on ASTM E−399 using a laser-cutting technique. A sub-sized tension sample based on ASTM E−8 was similarly fabricated using a rectangular bar with

dimensions 145 × 25 × 3 mm (length × breadth × thickness). The entire sample fabrication process is illustrated in Figure S9. A schematic of the CT specimen with dimensions (left) and the photograph of a real sample (right) are presented in Figure S10A, whereas the schematic of a tension specimen with dimensions (left) and the photograph of a real sample (right) are presented in Figure S10B. A fine pre-crack with a length of approximately 1 mm was introduced at the notched end of the CT specimen using low-stress fatigue cycles.

The CT specimen was installed in the special CT-type loading stage of an Instron-E3000 equipment, and the sample was exposed to UV light (INNOCURE2000, LICHTZEN, Republic of Korea) for charging. The sample was exposed to UV for 2 min, which is sufficient time to attain the saturation point, and a fracture test was performed under a crosshead speed of 0.05 mm/s. The UV light continuously illuminated the samples throughout the fracture process. The entire fracture process was recorded using a high-speed camera (SA-X, LEASPI, Japan) at a frame speed of 125 fps; a multi-channel data link (MCDL) was used to synchronize the load and displacement data from the Instron-E3000 equipment with images from the camera. The experimental setup is illustrated in Figure S11. A tension test was performed using the Instron-E3000 device equipped with a conventional tension grip under identical experimental conditions of UV lighting, crosshead speed, and high-speed imaging to complement the ML response in the CT specimen.

Evaluation of ML using the MATLAB code

MATLAB was used to automatically extract the facial brightness profile of the ML intensity, which included information on the coordinates of each pixel, using high-speed ML images. Further, the MATLAB code calculates K_P^{ML} in addition to identifying plastic crack tips from the processed ML profiles based on ML mechanics. The code contains a set of sections for executing important subjobs to instantaneously obtain K_P^{ML}. First, the maximum intensity point was determined for each frame, and it was considered as a crack tip in each frame. Then, contours were generated, after which the distances between the crack tip and several points on a given contour near the crack tip were measured. The corresponding angles of inclination of these lines to the crack axis were also measured. ML intensity contours were converted into their corresponding stresses using the ML–stress relationship. Using Equation 11, K_P^{ML} was determined using the least squares method, as mentioned in STAR Methods. The codes are available in Supplementary Code 1.

FEM simulation

Abaqus 2021 was used to simulate the elastoplastic crack tip and its K_P^{FEM} under quasi-dynamic fracture using FEM. The 3D CT specimens shown in Figure S12A are modeled with mechanical properties E = 2800 MPa, $\vartheta = 0.33$, and $\sigma_o = 22.8\ MPa$, obtained through uniaxial tension testing illustrated in Figure S13. The true stress and true strain in the uniaxial tension test were used in the model to ensure elastic–plastic fracture. Reference points R1 and R2 are created at the centers of the respective holes and coupled with the surfaces, as depicted in Figure S12B. The boundary conditions were applied at R1 and R2 such that R1 was constrained in all directions except for the movement along the y axis and rotation along the z axis, whereas R2 was constrained in all directions except rotation along the z axis. Figure S12C shows a 3D view of a crack and the direction of virtual crack extension, as indicated by the q-vector. A hex-dominated swept meshing technique was applied to the inner circular partitioned cell. The structure was modeled based on a 20-node quadratic-brick finite element (C3D20) for ensuring a singular stress field at the crack tip; a value of 0.25 was used for the mid-side node parameter. The results of the FEM simulations are presented in Figure S12D, where the effective stress field is illustrated. Finally, the J-integral obtained from the FEM model was subsequently converted to K_P^{FEM} based on Equation 12, as shown in the STAR Methods.

Learning for dual AI

The GAN (Pix2Pix), based on the open-source code and available at https://github.com/phillipi/pix2pix20, was reconstructed in Python (Version 3.6.6). The training and test sets for this GAN were prepared using ML images obtained from a high-speed camera; the corresponding FEM images were simulated using Abaqus. For a more dynamic training for cracking under CT, 300 paired images of ML and FEM immediately after crack initiation were carefully selected and resized to 256 × 256 × 3. In the case of the ML images, an additional mark used to notify the maximum intensity position was introduced using MATLAB 2018b for increasing both the learning efficiency and the accuracy. Then, the preprocessed dataset was trained for 300 epochs with a learning rate of 0.0002 and a momentum parameter of 0.5. Comparative learning was considered by restricting the dataset to 270 paired images to verify the performance of the trained

GAN; the testing was maintained for all 300 paired images for supplying fake images to testing the CNN models. The translation of image from one domain to another domain in the current work is less complicated for the powerful pix2pix GAN algorithm although the number of data is lower compared to that of a range of the conventional training dataset sizes, e.g., around 500–1,000 images for Pix2Pix-driven photo-to-street-map transition.[20] Indeed, the monotonous feature for our crack tip field images does not seem to require as many training images as other pix2pix-drive style alteration cases wherein more complicated features are considered. The training and testing datasets originated from completely separate photographs, and therefore, the possibilities of information leakage and overfitting during training are minimized.

The CNN model built to predict the PSIF from the GAN-generated images was also constructed in Python (Version 3.6.6) and built on Keras (Version 2.2.2), Pandas (Version 0.23.4), and Numpy (Version 1.14.5). The CNN model comprised five convolution and eight dense layers based on the mean squared error loss function and Adam optimizer. However, two identical models—forward and backward— were introduced separately to independently postulate the PSIFs from the fake ML and fake FEM images. The former was trained using real FEM images and K_P^{FEM}s, whereas the latter was optimized using empirical ML images and K_P^{ML}s. The learning procedures for both the forward and backward CNN models were continued for up to 300 epochs for minimizing the loss to the well below 0.00002. The forward and backward CNN models were tested with GAN generated fake FEM and fake ML images to predict the PSIFs.

Solution to determine PSIF from ML isointensity contours

Hutchinson[44] proposed a general working law in 1968 based on Williams's (1952) research[42] to address the mechanism of near-field stress distribution in the immediate vicinity of the crack tip of a nonlinear Ramberg–Osgood material that follows a general phenomenological power law model for uniaxial tensile behavior. Following Williams, Hutchinson proposed an asymptotic expansion of the solution for nonlinear materials in the form of a series of radii, given by

$$\varphi = r^s \widehat{\varphi}_1(\theta) + r^{s-1}\widehat{\varphi}_2(\theta) + \ldots, \quad \text{(Equation 1)}$$

where $\widehat{\varphi}_i$ $(i = 1, 2\ldots.)$ represents the angular variations of the stress tensor components; r and θ represent the polar coordinates; and $s = \frac{2n+1}{n+1}$, where n represents the strain-hardening component of the material.

When considering only the first term of the series and using the compatibility equation and Ramberg–Osgood relationship, the governing equations of various stress fields take the form

$$\sigma_e = \sigma_0 K_P r^{-\left(\frac{1}{n+1}\right)} \tilde{\sigma}_e(\theta, n) \quad \text{(Equation 2)}$$

$$\sigma_{rr} = \sigma_0 K_P r^{-\left(\frac{1}{n+1}\right)} \tilde{\sigma}_{rr}(\theta, n) \quad \text{(Equation 3)}$$

$$\sigma_{\theta\theta} = \sigma_0 K_P r^{-\left(\frac{1}{n+1}\right)} \tilde{\sigma}_{\theta\theta}(\theta, n) \quad \text{(Equation 4)}$$

$$\sigma_{r\theta} = \sigma_0 K_P r^{-\left(\frac{1}{n+1}\right)} \tilde{\sigma}_{r\theta}(\theta, n) \quad \text{(Equation 5)}$$

In the above equations, σ_o represents the yield stress; $\widehat{\sigma}_e(\theta, n)$ and σ_e denote the dimensionless effective stress and effective stress, respectively; and $\widehat{\sigma}_{ij}(\theta, n)$ and σ_{ij} represent the dimensionless stress tensor component and stress tensor component of the polar coordinate, respectively. Furthermore, K_P denotes the PSIF.

Shih (1973)[45] modified Equations 2–5 to address the nature of the loading conditions because mixed-mode loading conditions prevail in a real environment; thus, a new parameter, called the mixed-mode parameter (M_p) is incorporated such that $M_p = 0$ for mode I, $M_p = 1$ for mode II, and M_p lies between 0 and 1 for the mixed mode. Thus, the dimensionless effective stress depends on the value of M_p in addition to the polar coordinate and strain-hardening components. The modified expressions are given by

$$\sigma_e = \sigma_0 K_P r^{-\left(\frac{1}{n+1}\right)} \tilde{\sigma}_e(\theta, n, M_p) \quad \text{(Equation 6)}$$

$$\sigma_{rr} = \sigma_0 K_P r^{-\left(\frac{1}{n+1}\right)} \tilde{\sigma}_{rr}(\theta, n, M_p) \quad \text{(Equation 7)}$$

$$\sigma_{\theta\theta} = \sigma_0 K_P r^{-\left(\frac{1}{n+1}\right)} \tilde{\sigma}_{\theta\theta}(\theta, n, M_p) \quad \text{(Equation 8)}$$

$$\sigma_{r\theta} = \sigma_0 K_P r^{-\left(\frac{1}{n+1}\right)} \tilde{\sigma}_{r\theta}(\theta, n, M_p) \quad \text{(Equation 9)}$$

The ML intensity contours observed in the plastic zone were considered to be triggered by the effective stress, which can be easily obtained from the calibrated ML–stress relationship curve. However, the fourth-order differential equation in Equation 10 must be solved to determine $\tilde{\sigma}_e(\theta, n, M_p)$. This can be solved numerically (finite difference method) using the transformation to a system of first-order differential equations, as indicated in[46]

$$\left[n(s-2) - \frac{d^2}{d\theta^2}\right]\left[\tilde{\sigma}_e^{n-1}\left(s(s-3)\tilde{\varphi} - 2\frac{d^2\tilde{\varphi}}{d\theta^2}\right)\right] + n(s-2)[n(s-2)+1]\tilde{\sigma}_e^{n-1}\left[s(2s-3)\tilde{\varphi} - \frac{d^2\tilde{\varphi}}{d\theta^2}\right] + 6(s-1)[n(s-2)+1]\frac{d}{d\theta}\left(\tilde{\sigma}_e^{n-1}\frac{d\tilde{\varphi}}{d\theta}\right) = 0 \quad \text{(Equation 10)}$$

Finally, σ_e in Equation 6 can be replaced by σ_T to indicate that it can be obtained from the ML–stress relationship under the uniaxial tensional test; hence, Equation 6 can be reformulated using

$$\sigma_T = \sigma_0 K_P r^{-\left(\frac{1}{n+1}\right)} \tilde{\sigma}_e(\theta, n, M_p) \quad \text{(Equation 11)}$$

Equation 11 is the governing equation for the isochromatic fringes formed by ML emission inside the plastic zone in front of a crack in a homogeneous, isotropic, and elastic–plastic solid under the general mixed-mode plane stress condition. After the hardening exponent n is specified from the Ramberg–Osgood relationship, K_P and M_p can be used to characterize the plastic zone stress field completely.

Furthermore, as reported in the study by McClintock,[47] K_P can be related to the J-integral as

$$K_P = \left(\frac{J}{\alpha\sigma_0\varepsilon_0 I_n}\right)^{\frac{1}{n+1}}, \quad \text{(Equation 12)}$$

where ε_0, α, and I_n represent the yield strain corresponding to the yield stress ($\varepsilon_0 = \sigma_o/E$), Ramberg–Osgood constant, and numerical constant, respectively.